Thesis for the Degree of Licentiate of Technology

Modelling and Retrieval of Forest Parameters from Synthetic Aperture Radar Data

Maciej Jerzy Soja

CHALMERS

Department of Earth and Space Sciences
Chalmers University of Technology
Gothenburg, Sweden 2012

Modelling and Retrieval of Forest Parameters from Synthetic Aperture Radar Data
Maciej Jerzy Soja

Technical Report 51L,
Radar Remote Sensing Group
Department of Earth and Space Sciences
Chalmers University of Technology
SE–412 96 Gothenburg, Sweden
Phone: +46 (0)31 772 1000
E-mail: soja@chalmers.se

Cover: A gradual transition between two co-registered images of Remningstorp is shown. To the left, a biomass map estimated from P-band SAR using the model introduced in Paper A is shown. The SAR data were obtained within the BioSAR 2010 experiment (heading 200°). To the right, a Google Earth image of the same region is shown.

Printed by Chalmers Reproservice
Chalmers University of Technology
Gothenburg, Sweden 2012

"Genius is one percent inspiration,
ninety-nine percent transpiration."
Thomas Alva Edison (1847–1931)

dla dziadków Jasiów

Modelling and Retrieval of Forest Parameters from Synthetic Aperture Radar Data

Maciej Jerzy Soja
Department of Earth and Space Sciences
Chalmers University of Technology

Abstract

Currently, one of the most uncertain factors in the global carbon cycle models lies in the terrestrial carbon stock, mainly forests. The available methods for global forest resource mapping provide only rough estimates of biomass, the most relevant practical quantity related to carbon stock.

Spaceborne synthetic aperture radar (SAR) is a tool potentially suitable for global forest monitoring. As an active microwave sensor, SAR has the advantage of being independent of weather and external illumination. Spaceborne SAR can be designed for different frequencies and with resolutions as low as a few metres. Moreover, SAR systems operating at frequencies below L-band show good sensitivity to biomass. A spaceborne solution introduces also the possibility of frequent acquisitions, which is beneficial in applications such as detection of unlawful clear-cutting, storm damages, and forest fires.

In the first paper, a new biomass retrieval model for boreal forest using polarimetric, airborne P-band SAR backscatter is presented. The model is based on two main SAR quantities: the HV backscatter gamma nought and the HH/VV backscatter ratio, together with a topographic correction. Data from the two airborne experiments BioSAR 2007 and BioSAR 2008, performed in two distinct test sites Remningstorp and Krycklan, were used for this study. The model was compared to other, previously published models in a set of tests. In one of the tests, the models were evaluated across sites, i.e. training was done with data from one test site, and the models were validated using data from the other test site. Stand-wise root-mean-square errors of 40–59 tons/ha, or 22–32% of the mean biomass were observed for across-site validation.

In the second paper, a forward model for extended covariance matrix prediction for boreal forest in P-band SAR is presented. Data from BioSAR 2007 campaign were used for model derivation. The model is able to predict backscatter at HH, HV, and VV, together with the complex correlation between HH and VV, and complex correlation coefficients for three interferometric pairs (one for each polarisation). The forward model builds on a physical model and linear regression of BioSAR 2007 data. The model is further developed in the third paper. In the fourth paper, a tropical forest scenario is added, derived from the data acquired within the TropiSAR 2009 experiment.

In the fifth paper, spaceborne SAR is used to delineate wind-thrown trees and clear-cuts during a controlled experiment conducted in the test site of Remningstorp in 2009. Data from three satellites were used: ALOS PALSAR (L-band), RADARSAT-2 (C-band), and TerraSAR-X (X-band). The detection capabilities vary for the different satellites due to different resolutions, and also due to different scattering properties. It is observed, that TerraSAR-X is suitable for storm damage detection due to its high resolution. ALOS PALSAR is suitable for detection of clear-cuts due to its sensitivity to biomass.

Keywords: synthetic aperture radar (SAR), forest, biomass estimation, modelling

Appended papers

This thesis is based on the following papers:

Paper A: **M. J. Soja**, G. Sandberg, and L. M. H. Ulander. Biomass Retrieval for Boreal Forests using P-band SAR Backscatter. Submitted to *IEEE Transactions on Geoscience and Remote Sensing*, February 2012.

Paper B: **M. J. Soja** and L. M. H. Ulander. A Hybrid Model for Interferometric and Polarimetric P-band SAR Imaging of Forests. *Proceedings for "PolInSAR 5th International Workshop on Science and Applications of SAR Polarimetry and Polarimetric Interferometry"*, Frascati, Italy, 24–28 January 2011 (ESA SP-695, March 2011).

Paper C: **M. J. Soja**. Forward Model for Interferometric and Polarimetric P-band SAR Imaging of Forests. Manuscript submitted to DLR as a part of the WP20 Report for the ESA project *Development of Algorithms for Forest Biomass Retrieval*, June 2011.

Paper D: **M. J. Soja**. Tropical Forest Update to Paper C. Manuscript submitted to DLR as annex to Paper C, September 2011.

Paper E: L. E. B. Eriksson, J. E. S. Fransson, **M. J. Soja**, and M. Santoro. Spaceborne SAR for detection of boreal wind-thrown forest and clear-cuts. Submitted to *Remote Sensing of Environment*, August 2011.

Related papers

The following papers are related to the work presented in this thesis, but they have not been appended:

Paper 1: **M. J. Soja**, G. Sandberg, and L. M. H. Ulander. Topographic Correction for Biomass Retrieval from P-band SAR Data in Boreal Forests. *Proceedings of IEEE International Geoscience and Remote Sensing Symposium (IGARSS)*, Honolulu, HI, USA, 25–30 July 2010, pp. 4776–4779.

Paper 2: J. E. S. Fransson, A. Pantze, L. E. B. Eriksson, **M. J. Soja**, and M. Santoro. Mapping of windthrown forests using satellite SAR images. *Proceedings of IEEE International Geoscience and Remote Sensing Symposium (IGARSS)*, Honolulu, HI, USA, 25–30 July 2010, pp. 1242–1245.

Paper 3: G. Sandberg, **M. J. Soja**, and L. M. H. Ulander. Impact and Modeling of Topographic Effects on P-band SAR Backscatter from Boreal Forests. *Proceedings of IEEE International Geoscience and Remote Sensing Symposium (IGARSS)*, Vancouver, BC, Canada, 24–29 July 2011, pp. 3522–3525.

Paper 4: L. M. H. Ulander, G. Sandberg, and **M. J. Soja**. Biomass retrieval algorithm based on P-band BioSAR experiments of boreal forest. *Proceedings of IEEE International Geoscience and Remote Sensing Symposium (IGARSS)*, Vancouver, BC, Canada, 24–29 July 2011, pp. 4245–4248.

Paper 5: L. M. H. Ulander, A. Gustavsson, P. Dubois-Fernandez, X. Depuis, J. E. S. Fransson, J. Holmgren, J. Wallerman, L. E. B. Eriksson, G. Sandberg, and **M. J. Soja**. BioSAR 2010 — A SAR Campaign in Support to the BIOMASS Mission. *Proceedings of IEEE International Geoscience and Remote Sensing Symposium (IGARSS)*, Vancouver, BC, Canada, 24–29 July 2011, 1528–1531.

Acknowledgements

First and foremost, I would like to thank my supervisor and mentor, Lars Ulander, for making the writing of this thesis possible. Thank you for your guidance and support. Thank you for the countless hours spent on reading and correcting my papers.

★

Also, I would like to thank my two assistant supervisors: Leif Eriksson and Johan Fransson, for being there for me whenever necessary. Also, thank you, Leif, for being a great leader for the Radar Remote Sensing group. Thanks to you, the atmosphere in the group is outstanding.

★

I would like to dedicate special thanks to Gustaf Sandberg and Anders Berg, my superb colleagues and friends. Thank you for being my sounding board, for your feedback and input. Thank you for your constant support. Thank you for making this thesis so much better.

★

Many thanks to my current and former colleagues from the Radar Remote Sensing Group, Jan Torgrimsson, Gisela Carvajal, Annelie Wyholt, and Jan Askne, as well as Mattias Andersson and Maurizio Santoro, for all the fruitful discussions, helpful comments, and valuable input. Thank you for your contribution to the great atmosphere in our group.

★

Special thanks to Donal, Marston, and Matthew, for being my good friends and my English gurus. Many thanks to all my other colleagues and staff from the department of Earth and Space Sciences. Thank you all for keeping the department wheels in motion and for making the coffee breaks very enjoyable.

★

Additionally, I would like to express my gratitude to my colleagues from the German Aerospace Center (DLR), Kostas Papathanassiou, Stefan Sauer, Florian Kugler, and Seung-Kuk Lee, for their help during our joint projects. I am very thankful for your time and dedication. I am looking forward to further cooperation with you all.

★

I would also like to thank Swedish National Space Board (SNSB) and European Space Agency (ESA) for the funding of my research.

★

Thank you, my loving and beloved family, for providing motivation and support whenever needed. Thank you, my awesome friends, for enlightening the darkness during winters and for making the summer days less rainy. I love you all!

Contents

Chapter 1

Introduction

1.1 Forests in Environment and Human Society

Forests play a vital role in Earth's ecosystems. Through the process of photosynthesis, trees and plants bind CO_2 from the atmosphere, part of which is transformed into carbon stock. Forests provide shelter to countless animal and vegetation species, housing around 80 % of the terrestrial biodiversity [1]. They also take part in the water cycle, prevent soil from erosion, clean water and air from pollutants, etc. At the same time, forests are one of our greatest natural resources. Timber is used as a construction material, for paper production, and as a fuel. Animals and vegetation provide food. Forests also have great recreational values.

Until quite recently, the global effects of human exploitation of forests were negligible due to a small population and low demand, and inefficient harvesting methods. However, as the human population grew rapidly, the demand on forest products increased. With the advent of industrialisation, the harvesting methods became more efficient, and fossil fuels such as coal, gas, and oil became essential to the society. Only in the late 20th century, the first signs of a possible human influence on the global ecosystem were observed. Acid rain, ozone depletion, and global warming are just a few, potentially human-induced threats. Presently, the public awareness of the climate problems is increased, the first measures are taken, and a lot of research is centred around Earth system science and climate change (see [2] and references therein).

One of the greatest concerns is the influence of deforestation on global carbon dioxide emissions. During the last 50 years, a steady increase of the atmospheric CO_2 has been observed [3, 4]. Some sources state, that as much as 20 % of the global carbon dioxide emissions come from deforestation [2, 5]. However, the exact effect of deforestation is unknown. The single largest uncertainty in the current carbon cycle models lies in the terrestrial carbon sink, mainly forests [4]. The most relevant, measurable quantity directly related to the carbon distribution in biosphere is biomass, the mass of the organic matter living in a certain region. Since forests account for over 80 % of the terrestrial above ground biomass, and around 50 % of biomass is carbon [6], accurate, global forest biomass maps are required to improve global carbon cycle modelling. The possibility of periodic updates should also exist in order to be able to detect unlawful deforestation, aid disaster handling, and improve forest management.

1.2 Remote Sensing of Forests

Since forests cover more than 31 % of Earth's total land surface [1], satellite remote sensing is the only applicable method for frequent, global biomass mapping. This can be done in several ways. Optical methods have long been used for this task. However, these methods are inaccurate and sensitive to weather conditions [6]. This is especially problematic around the equator, where most of the high-biomass tropical rainforests are situated, but also where the cloud cover is the most persistent. Small-footprint lidar scanning is currently the most accurate method for remote forest mapping [7]. However, spaceborne application of this technique is difficult, mostly due to complications such as large footprint and low coverage [6].

Synthetic aperture radar (SAR) does not suffer from the same disadvantages as the optical and lidar

sensors. As an active microwave sensor, SAR carries its own illumination and is weather independent. Thanks to the synthetic aperture technique, the resolution of a spaceborne SAR system can be of the order of metres. Moreover, many studies show that P-band SAR (around 0.22–0.45 MHz) is suitable for forest biomass mapping [8–20]. Although SAR mapping at VHF-band gives even better results, as shown by the CARABAS-system operational at 20–90 MHz (see [21] and references therein), the large ionospheric influence makes the VHF-band unsuitable for spaceborne use [22].

Spaceborne use of P-band SAR has previously been impossible due to frequency restrictions. However, after the World Radiocommunication Conference in 2003, a narrow band within the P-band has been opened for secondary use (432–438 MHz, wavelengths around 69 cm). A fully polarimetric P-band SAR satellite system called BIOMASS has been proposed to European Space Agency (ESA) for the 7th Earth Explorer mission [19, 23, 24]. The major part of the work presented in this thesis has been done within the feasibility study for this mission.

1.3 Outline of this Thesis

This thesis is concentrated on SAR imaging of forests. It is structured as follows:

- In Chapter 2, the basic radar and SAR theory is presented. The most important equations dealing with resolution, ranging, and Doppler measurements are explained. Some examples of SAR imagery are shown, and the differences between SAR and optical imaging are pointed out. SAR polarimetry and interferometry are also introduced. Different scattering mechanisms are described.
- In Chapter 3, the appended papers are presented. In Paper A, biomass retrieval from P-band SAR is assessed. In Papers B, C, and D, a forward model for polarimetric and interferometric P-band SAR modelling is presented. In Paper E, storm damage and clear cut detection at L-, C-, and X-band with spaceborne SAR is evaluated.
- In Chapter 4, the thesis is summed up and conclusions are drawn. Some ideas for future work are also mentioned.

Chapter 2

Synthetic Aperture Radar Principles

2.1 Radar Basics

Radar stands for ***ra****dio* ***d****etection* ***a****nd* ***r****anging* [25,26]. Although the term "radar" was first introduced by the US Navy in 1940, the development of radar started in the beginning of the 20th century. Radar was initially used, as the name suggests, only for detection and ranging of military targets. Nowadays, the functions of radar extend far beyond that, including velocity measurements, shape and size determination of objects, angular measurements, 2- and 3-dimensional mapping, etc. Radar applications include parking assistance in cars, traffic speed measurements, airport surveillance, rain rate mapping and weather monitoring, missile detection, missile guidance, earth observations from satellites, satellite and space debris monitoring from ground, and many others.

Radar is an active remote sensing technique in which an electromagnetic (EM) signal is transmitted, and the reflected echoes are detected and studied[1]. Advantages of radar are many. Since radar is an active system, no external illumination is needed. Also, the terrestrial atmosphere is almost transparent to EM waves with frequencies between a few hundred MHz and approximately 10 GHz [27]. In practice, this means that most radar systems are unaffected by clouds, rain, wind, etc. Also, the choice of frequency gives many possibilities. High frequency means in general better resolution, but small penetration depth. At lower frequencies, penetration capabilities are better, thus making it possible to uncover objects invisible with traditional optical methods. The trade-off is lower resolution and larger antennas. Radar systems are primarily classified by the frequency band used. In Table 2.1, the most commonly used frequency bands are presented.

The transmitted signal usually has a well-determined polarisation, that is the orientation of EM wave oscillations. The returning signal is then measured at a certain polarisation. If the transmission is done with a horizontally polarised antenna (H), and the reception is done with a vertically polarised antenna (V), the polarisation mode is then called VH. Similarly, HH means that horizontally polarised antennas are used both for transmission and reception. If a system is capable of measuring all four combinations (HH, HV, VV, and VH) at the same time, together with their phase information, it is called *fully polarimetric*. If transmission and reception are both done with the same antenna, the radar system is called *monostatic*. In case of two separate antennas, the system is called *bistatic*. Throughout this work, only monostatic systems are used.

In radar imaging, the position of a target is determined by its *range* and *azimuth* (or *cross-range*) positions. Azimuth is the along-track position. *Slant range* is the line-of-sight distance between the antenna

[1]The principles of radar can be compared to echolocation, which is a navigation technique based on ultrasound sensing, used by bats and toothed whales in optically thick environments. Also sonar works similarly to radar, using sound waves in water (hydroacoustics).

phase centre and the target. *Ground range* is the corresponding distance projected to the ground. These dimensions are illustrated in Figure 2.1 and Figure 2.2.

2.1.1 Ranging, Radar Equation, and Radar Cross Section

The ranging technique using radar is straightforward. If the time between transmission and reception of a pulse is T, then the corresponding distance is [26]:

$$R = \frac{cT}{2}, \tag{2.1}$$

where the factor of 2 accounts for the two-way propagation, and c is the propagation velocity of EM waves in the propagation medium. In most radar applications, the latter is air and $c = c_0$ can be assumed, where c_0 is the speed of light in vacuum.

The ratio of the received and transmitted power (P_r and P_t, respectively) for a monostatic radar system is given by the *radar equation* [26, 29]:

$$\frac{P_r}{P_t} = \frac{\sigma\lambda^2 G^2}{(4\pi)^3 R^4 L}, \tag{2.2}$$

where σ is the *radar cross section* (RCS) of the object, λ is the wavelength, G is the gain of the antenna, and L is a factor representing losses. In most practical applications, P_t, λ, G, and L are known system parameters, R is computed from time delay according to (2.1), P_r is measured at the antenna. The estimation of RCS, the main observable in a radar system, is then straightforward. In cases when some system parameters are unknown, a calibration procedure needs to be performed first, using objects with known RCS.

A formal definition of RCS, or σ in (2.2) is [29]:

$$\sigma = \lim_{R\to\infty} 4\pi R^2 \frac{|\mathbf{E}^s|^2}{|\mathbf{E}^i|^2}, \tag{2.3}$$

where $\mathbf{E}^i$ and $\mathbf{E}^s$ are the incident and scattered electric fields, respectively, of the corresponding plane waves. The unit is m^2. RCS describes the effective cross section area of the target as it appears to the radar. RCS depends not only on the dielectric properties and the shape of the target, but also on system parameters, such as polarisation, angle of incidence, and frequency. RCS does not have to be related to the physical size of the studied object. Only for a perfect metallic sphere, and wavelengths much shorter than the dimensions of the sphere, RCS and the geometrical cross section area match exactly.

2.1.2 Range and Azimuth Resolutions

The simplest pulsed radar systems use monochromatic signals to create the transmitted pulses. The range resolution is in that case [26]:

$$\Delta R = \frac{c\tau}{2}, \tag{2.4}$$

where τ is the pulse length. Obviously, the resolution is dependent on the pulse length, and short pulses are more desirable. However, to keep the signal-to-noise ratio high, each pulse has to be either very powerful or long. A trade-off has to be made, which generally results in poor range resolution. Therefore, most modern

Table 2.1: Radar frequency band as defined in [28]. Note: P-band is an older band designation, and does not belong to the IEEE Standard.

Band:	Frequency range:
VHF	30–300 MHz
UHF	300–1000 MHz
L	1–2 GHz
S	2–4 GHz
C	4–8 GHz
X	8–12 GHz
P	*216–450 MHz*

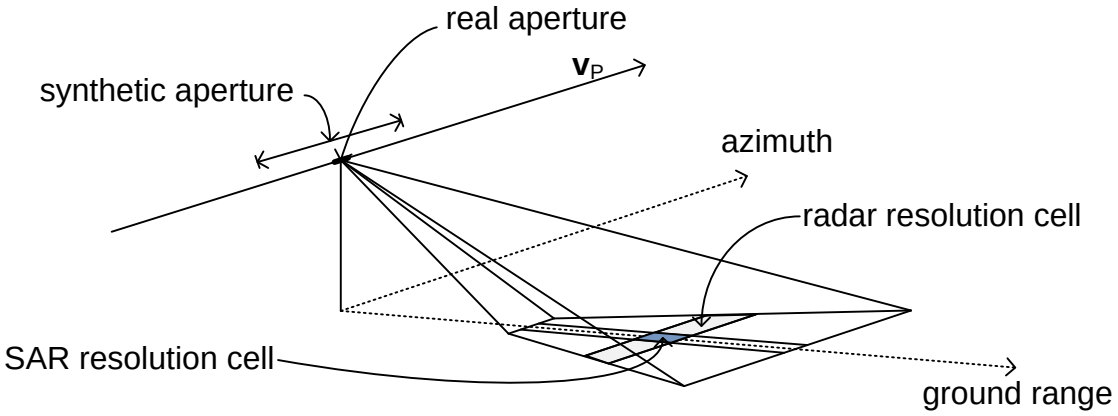

Figure 2.1: Basic SAR geometry under flat-earth approximation. The figure illustrates the principle of synthetic aperture. By synthesising a larger antenna, the resolution cell becomes smaller in azimuth.

radar systems use frequency-modulated pulses instead. This way, the transmitted energy can be distributed over many frequency components, and the effective pulse length can be shortened. For such a system, the range resolution is [25, 29]:

$$\Delta R = \frac{c}{2B}, \tag{2.5}$$

where B is the bandwidth of the pulse. The central frequency of the signal is $f_c = c/\lambda$, where λ is the wavelength.

Two- and three-dimensional imaging can be achieved by sweeping the radar antenna over different directions. If a radar antenna has size D such that:

$$D \gg \lambda, \tag{2.6}$$

then the approximate beamwidth of the antenna can be computed as:

$$\Delta\phi \approx \frac{\lambda}{D}, \tag{2.7}$$

and the size of the illuminated region at distance R is then [29]:

$$\Delta x \approx \Delta\phi R \approx \frac{\lambda R}{D}. \tag{2.8}$$

As it can be observed, Δx depends on both range and antenna size. In order to get a good resolution at long distances, a large antenna is necessary.

2.1.3 Velocity Measurements

Radar systems may be coherent, which means that the phase of the transmitted signal is well known. If a scatterer positioned within the antenna beam is moving radially relative the antenna, a frequency shift will occur. The received signal will have slightly higher frequency if the object is moving towards the antenna, and vice versa. This effect is known as *Doppler shift*[2]. The *Doppler frequency*, that is the frequency shift compared to the nominal carrier frequency, is related to the relative radial velocity v of the scatterer as [29]:

$$f_D = -\frac{2v}{\lambda}. \tag{2.9}$$

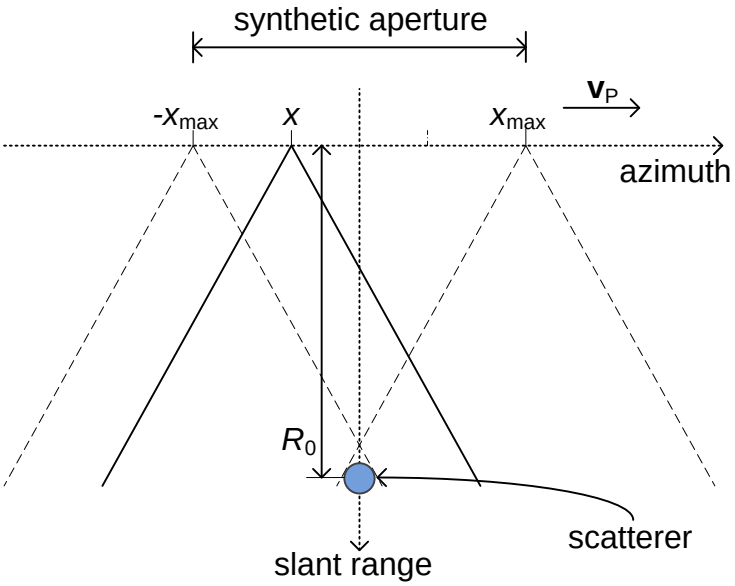

Figure 2.2: Basic SAR geometry seen in the slant range plane. A set of radar measurements is performed by an antenna moving at a constant velocity $\mathbf{v}_P$. At each position, the radial velocity of a stationary scatterer relative the antenna is different.

2.2 Synthetic Aperture Radar

As mentioned in Section 2.1.2, high azimuth resolution in radar requires very large antennas. Such antennas are difficult to design and impractical. In reality, a different approach called *synthetic aperture radar* (SAR) is used for high-resolution radar imaging.

The main idea of SAR is to synthesise a large antenna using multiple acquisitions made with a smaller antenna moving along a known path, see Figure 2.1. A small antenna has a large beamwidth, thus covering a large area on the ground. Each scatterer on the ground is then covered by several consecutive radar acquisitions, each from a different position along the track, see Figure 2.2. The magnitude of the Doppler shift induced by the relative motion depends on the azimuth position of each scatterer. Hence, a Doppler bandwidth is created. Azimuth resolution can now be improved much in the same way as range resolution was improved with the use of frequency-modulated pulses. A short derivation of SAR azimuth resolution is here presented. See also [30].

2.2.1 Resolution

Assume that a stationary scatterer is positioned at range R_0. The position of the antenna at time t is $x = v_P t$, where v_P is the velocity of the radar platform, see Figure 2.2. In the derivation that follows, it is assumed that the boresight (maximum gain) of the antenna is always perpendicular to the velocity vector of the platform (zero squint angle), and that the antenna moves along a straight path. The start-stop approximation is also assumed. Moreover, the imaged area on the ground is assumed to be perfectly flat (flat-earth approximation).

The instantaneous distance to the scatterer is:

$$R(t) = \sqrt{R_0^2 + (v_P t)^2} \approx R_0 \left(1 + \frac{(v_P t)^2}{2R_0^2}\right) \tag{2.10}$$

[2]Doppler shift can be easily observed in everyday life, for example when an ambulance is passing. The frequency of the siren is higher when the ambulance is approaching than when it is leaving.

and the velocity of the scatterer relative the antenna can be computed from (2.10) as:

$$v = \frac{\mathrm{d}R(t)}{\mathrm{d}t} = \frac{v_P^2 t}{R_0}, \tag{2.11}$$

The relative radial movement of the scatterer induces a Doppler shift. The Doppler frequency of this scatterer can be computed using (2.11) in (2.9):

$$f_D(t) = -\frac{2v_P^2 t}{\lambda R_0}, \tag{2.12}$$

where v_P is the velocity of the radar platform. The last time at which the antenna lobe covers the scatterer is $t_{\max}$, and can be computed from the expression for the approximate antenna beamwidth (2.7):

$$t_{\max} = \frac{x_{\max}}{v_P} \approx \frac{\lambda R_0}{2D_x v_P}, \tag{2.13}$$

where $D_x \gg \lambda$ is the antenna size in azimuth direction. Assuming the simplified geometry used in Figure 2.2 (flat earth and zero squint angle), the Doppler bandwidth can be computed as twice the magnitude of the highest Doppler frequency. Using (2.12) and (2.13), the Doppler bandwidth becomes:

$$B_D = 2|f_D(t_{\max})| = \frac{2v_P}{D_x}. \tag{2.14}$$

Equivalently with the expression in (2.5), the azimuth resolution can be computed using Doppler bandwidth B_D and platform velocity v_P:

$$\Delta x = \frac{v_P}{B_D} = \frac{D_x}{2}, \tag{2.15}$$

which means that the azimuth resolution of a SAR image can be as good as half the size of the antenna. Moreover, the resolution is not range dependent.

The SAR mode presented above, with fixed antenna direction, is called *stripmap SAR*. In *spotlight SAR*, the antenna is focussed on the same point along the whole synthetic aperture, giving better spatial resolution, but lower coverage. In *scan SAR*, the antenna beam is swept, which results in better coverage than stripmap at the price of resolution. See [29, 31, 32] for more information.

2.2.2 Image Characteristics

At a first glance, SAR images may remind of the more familiar optical images. However, the two imaging methods are conceptually different. This should be taken into consideration when studying SAR images.

The first difference between SAR images and optical images is the illumination. While SAR provides its own illumination, which can be easily controlled, optical imagery in remote sensing relies on solar illumination. In this meaning, SAR imagery is more predictable and reproducible. However, SAR imagery is also prone to other types of geometric distortions. In topographic terrain, effects such as layover and foreshortening show up [29]. Both in SAR imaging and optical imaging, the effects of shadow can be seen in non-illuminated regions.

Another difference comes with the way in which images are resolved. Optical imagery features constant resolution angle in both range and azimuth direction. Far-range pixels are therefore resolved with lower resolution than the ones in the near-range. In SAR, pixels are resolved at constant slant-range resolution. When projected on the ground, pixels in far-range have better resolution than those in near-range (assuming flat earth). In azimuth, all pixels have the same resolution (provided that the bandwidth is small compared to the central frequency). See Figure 2.3(a) for a schematic explanation.

While in optical imagery, incoherent radiation is used (the phase of sunlight is random), SAR uses coherent waves. This results in an effect called *speckle*. This effect occurs when more than one scatterer is located within a resolution cell at different distances from the radar. The total reflected wave will be a coherent sum of the waves reflected from each scatterer separately. The interaction of the waves will cause interference. The intensity will vary from pixel to pixel and the phase and amplitude of the reflected radiation will be random. This phenomenon is illustrated in Figure 2.3(b). In Figure 2.4, speckle can be easily observed. One way to reduce speckle effect is by *multilooking*, that is by spatial averaging. However, multilooking degrades the resolution of the image.

Electromagnetic waves interact strongly with objects with sizes comparable to, or larger than the wavelength. For visible light, wavelengths are around 400–700 nm, while for radio waves and microwaves, wavelengths can vary between millimetres and tens or even hundreds of metres. Objects with sizes smaller than

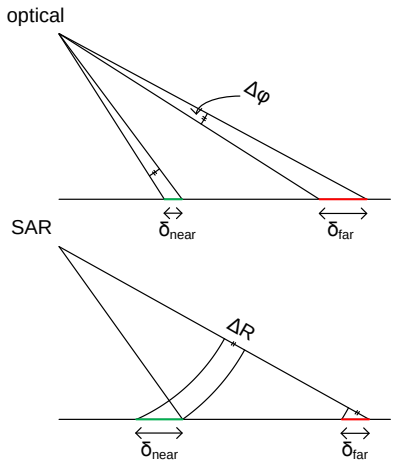

(a) Comparison of the size of the resolution cells in SAR and optical imaging under flat-earth assumption.

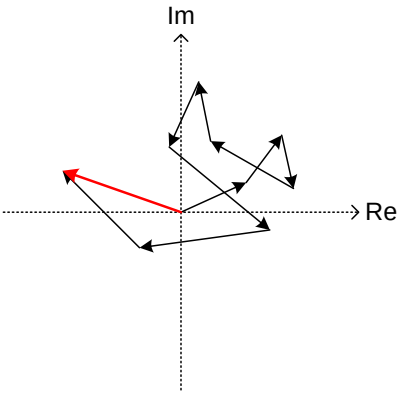

(b) The effect of speckle. Multiple scatterers within a resolution cell cause interference between the scattered waves.

Figure 2.3: Illustration of two principal differences between SAR and optical imagery.

(a) ALOS PALSAR (L-band, 14 MHz@1.3 GHz, date: 2008/08/20, mode: FBD, pol: HH, pixel size: 25 m x 25 m, approx. 7 looks/pixel, inc. angle: 34°, asc. orbit)

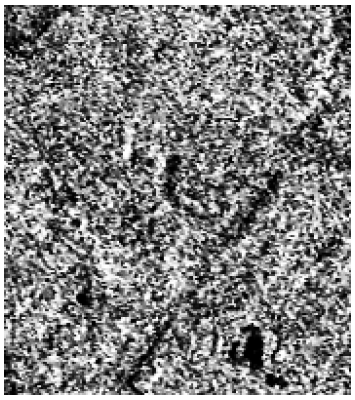

(b) RADARSAT-2 (C-band, 30 MHz@5.4 GHz, date: 2009/08/13, mode: FQ, pol: HH, pixel size: 10 m x 10 m, approx. 1.4 looks/pixel, inc. angle: 37°, desc. orbit)

(c) TerraSAR-X (X-band, 150 MHz@9.6 GHz, date: 2009/08/26, mode: HS, pol: HH, pixel size: 5 m x 5 m, approx. 11 looks/pixel, inc. angle: 34°, desc. orbit)

Figure 2.4: The same region imaged by three different satellites at three different frequencies (the first number is the bandwidth, the second number is the central frequency). The size of the imaged area is 1.78 km x 2.00 km Note: for ALOS PALSAR, no suitable image was available for the same date and orbit type. The shown image comes from the same season, a year earlier than for the two other satellites. Also, the image was acquired in ascending orbit, which means that the acquisition was made from the opposite direction.

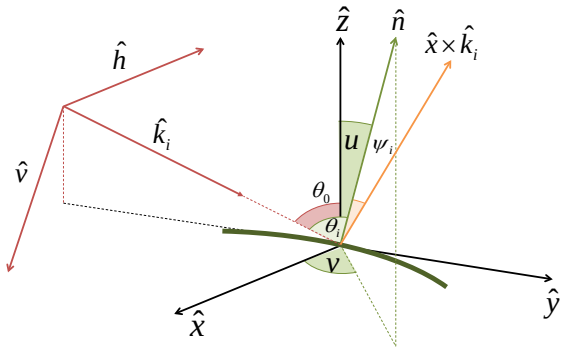

Figure 2.5: Basic geometry of scattering. $\hat{\mathbf{n}}$ *is the ground surface normal.* $\hat{\mathbf{x}} \times \hat{\mathbf{k}}_i$ *is the imaging plane normal.*

the wavelength are in the Rayleigh regime and interact weakly. SAR imagery can therefore "see through" objects that normally block visible light. Depending on the wavelength, different features of the imaged region can be observed. In Figure 2.4, a forested region is imaged at three different wavelengths in approximately the same conditions (23 cm for L-band, 5.6 cm for C-band, and 3.1 cm for X-band). The three images all have different resolution, but also the scattering behaviour is different. Some regions that appear bright at L-band, are dark at X-band. By imaging at different frequencies, different features of the same region can be extracted.

2.2.3 Polarimetry and Interferometry

A fully polarised EM wave propagating in the direction of $\hat{\mathbf{k}}_i$, see Figure 2.5, can be expressed as a sum of two components, one in the horizontal direction and one in the vertical direction:

$$\mathbf{E} = E_{\mathrm{H}}\hat{\mathbf{h}} + E_{\mathrm{V}}\hat{\mathbf{v}}, \tag{2.16}$$

where

$$\hat{\mathbf{h}} = \frac{\hat{\mathbf{z}} \times \hat{\mathbf{k}}_i}{|\hat{\mathbf{z}} \times \hat{\mathbf{k}}_i|}$$

is the horizontal unit vector, perpendicular both to the vertical direction and to the direction of propagation, and

$$\hat{\mathbf{v}} = \hat{\mathbf{h}} \times \hat{\mathbf{k}}_i$$

is the vertical unit vector, perpendicular to both the horizontal direction and the direction of propagation, see also Figure 2.5. Equivalently, the electric field can be written as a *Jones vector* [33]:

$$\mathbf{E} = \begin{bmatrix} E_{\mathrm{H}} \\ E_{\mathrm{V}} \end{bmatrix}. \tag{2.17}$$

Assuming plane waves, the incident electric field ($\mathbf{E}^i$) and the scattered electric field ($\mathbf{E}^s$) are now related through:

$$\mathbf{E}^s = \frac{\mathrm{e}^{ik_0 R}}{R}\,[S]\,\mathbf{E}^i \tag{2.18}$$

or

$$\begin{bmatrix} E^s_{\mathrm{H}} \\ E^s_{\mathrm{V}} \end{bmatrix} = \frac{\mathrm{e}^{ik_0 R}}{R} \begin{bmatrix} S_{\mathrm{HH}} & S_{\mathrm{HV}} \\ S_{\mathrm{VH}} & S_{\mathrm{VV}} \end{bmatrix} \begin{bmatrix} E^i_{\mathrm{H}} \\ E^i_{\mathrm{V}} \end{bmatrix}, \tag{2.19}$$

where R is the distance between the target and the antenna, $k_0 = 2\pi/\lambda$ is the wavenumber, and $[S]$ is the complex 2×2 *scattering matrix*. The scattering matrix fully describes scattering from the target at the governing radar setup (frequency, incident angle). For monostatic radar, $S_{\mathrm{HV}} = S_{\mathrm{VH}}$ due to reciprocity [34].

In remote sensing, most scatterers are not stable, fixed point targets, but they are distributed, dynamic targets stochastically changing in time and space. Such targets are best described using second order moments.

The scattering vector in the lexicographic basis for a SAR image is defined as [33]:

$$\underline{\mathbf{\Omega}} = \left[S_{\mathrm{HH}},\ \sqrt{2}S_{\mathrm{HV}},\ S_{\mathrm{VV}}\right]^{\mathrm{T}}, \tag{2.20}$$

where $^{\mathrm{T}}$ is the transpose operator. The factor $\sqrt{2}$ is introduced to keep the total power invariant after omitting the redundant element S_{VH}. The scattering vector is introduced to enable the use of matrix algebra in further operations.

Polarimetric SAR

If a SAR system is fully polarimetric, that is if it can measure the three elements of $\underline{\mathbf{\Omega}}$ in terms of magnitude and phase, then the *polarimetric covariance matrix* can be computed [33]:

$$[V] = \left\langle \underline{\mathbf{\Omega}} \cdot \underline{\mathbf{\Omega}}^{\mathrm{H}} \right\rangle = \begin{bmatrix} \langle |S_{\mathrm{HH}}|^2 \rangle & \sqrt{2}\langle S_{\mathrm{HH}} S_{\mathrm{HV}}^* \rangle & \langle S_{\mathrm{HH}} S_{\mathrm{VV}}^* \rangle \\ \sqrt{2}\langle S_{\mathrm{HV}} S_{\mathrm{HH}}^* \rangle & 2\langle |S_{\mathrm{HV}}|^2 \rangle & \sqrt{2}\langle S_{\mathrm{HV}} S_{\mathrm{VV}}^* \rangle \\ \langle S_{\mathrm{VV}} S_{\mathrm{HH}}^* \rangle & \sqrt{2}\langle S_{\mathrm{VV}} S_{\mathrm{HV}}^* \rangle & \langle |S_{\mathrm{VV}}|^2 \rangle \end{bmatrix}, \tag{2.21}$$

Where $^{\mathrm{H}}$ is the Hermitian (conjugate transpose) operator. Note, that the elements on the diagonal are real valued, and they represent backscatter intensities for the three polarisations. The *backscattering coefficient sigma nought* for polarisation mode PQ can be defined and expressed in terms of the diagonal elements in (2.21) using (2.3) and (2.18):

$$\sigma^0_{\mathrm{PQ}} = \frac{\langle \sigma_{\mathrm{PQ}} \rangle}{A_{GR}} = \frac{4\pi \langle |S_{\mathrm{PQ}}|^2 \rangle}{A_{GR}} = \frac{4\pi \cos\psi_i \langle |S_{\mathrm{PQ}}|^2 \rangle}{A_{SR}}, \tag{2.22}$$

where A_{SR} is the area of a resolution cell in slant range, A_{GR} is the area of a resolution cell in ground range, ψ_i is the angle between the ground surface normal and image plane normal, as defined in [35] and in Figure 2.5. The factor $\cos\psi_i$ projects the resolution cell on the ground.

Using polarimetric SAR (PolSAR) imagery, scattering mechanisms occurring in the imaged region can be studied, often using *polarimetric decompositions*. In this approach, the covariance matrix (or the similar coherency matrix) is decomposed into several matrices, each representing a certain, well defined scattering mechanism (such as direct backscatter, dihedral reflection, and random volume scattering, see Section 2.3). There are many different decomposition theorems based on different principles. Consult [33, 36] for more information.

Three civilian, spaceborne, fully polarimetric SAR systems have been launched, SIR-C/X (USA, Germany, Italy), ALOS PALSAR (Japan) and RADARSAT-2 (Canada), of which only the last one is still operational. Some fully polarimetric airborne SAR systems include: NASA/JPL AIRSAR and UAVSAR (USA), DLR ESAR (Germany), and ONERA RAMSES and SETHI (France). A description of the past and present polarimetric SAR systems can be found in [33].

Interferometric SAR

Assume that two fully polarimetric SAR images are acquired from two positions separated either by a spatial baseline $\mathbf{B}$ or a temporal baseline B_T, see Figure 2.6. The scattering vectors of the two images are $\underline{\mathbf{\Omega}}_1$ and $\underline{\mathbf{\Omega}}_2$. The *interferometric covariance matrix* for this pair is [33]:

$$[K_{12}] = \left\langle \underline{\mathbf{\Omega}}_1 \cdot \underline{\mathbf{\Omega}}_2^{\mathrm{H}} \right\rangle = \begin{bmatrix} \langle S^1_{\mathrm{HH}} S^{2*}_{\mathrm{HH}} \rangle & \sqrt{2}\langle S^1_{\mathrm{HH}} S^{2*}_{\mathrm{HV}} \rangle & \langle S^1_{\mathrm{HH}} S^{2*}_{\mathrm{VV}} \rangle \\ \sqrt{2}\langle S^1_{\mathrm{HV}} S^{2*}_{\mathrm{HH}} \rangle & 2\langle S^1_{\mathrm{HV}} S^{2*}_{\mathrm{HV}} \rangle & \sqrt{2}\langle S^1_{\mathrm{HV}} S^{2*}_{\mathrm{VV}} \rangle \\ \langle S^1_{\mathrm{VV}} S^{2*}_{\mathrm{HH}} \rangle & \sqrt{2}\langle S^1_{\mathrm{VV}} S^{2*}_{\mathrm{HV}} \rangle & \langle S^1_{\mathrm{VV}} S^{2*}_{\mathrm{VV}} \rangle \end{bmatrix}, \tag{2.23}$$

where S^i_{PQ} is the complex scattering amplitude for polarisation PQ and image i, and * is the conjugate operator. Assume also that the difference in incident angles between the two acquisitions is small (same scattering mechanisms), and that the resolution cells cover each other (same speckle effect). The elements on the diagonal of $[K_{12}]$ are called *interferograms*. Interferogram phase is an indicator of the change in distance between the two acquisitions [36]:

$$\Delta\phi = \arg\left(\langle S^1_{\mathrm{PQ}} \cdot S^{2*}_{\mathrm{PQ}} \rangle\right) = \frac{4\pi}{\lambda} \cdot \Delta R + 2\pi n, \tag{2.24}$$

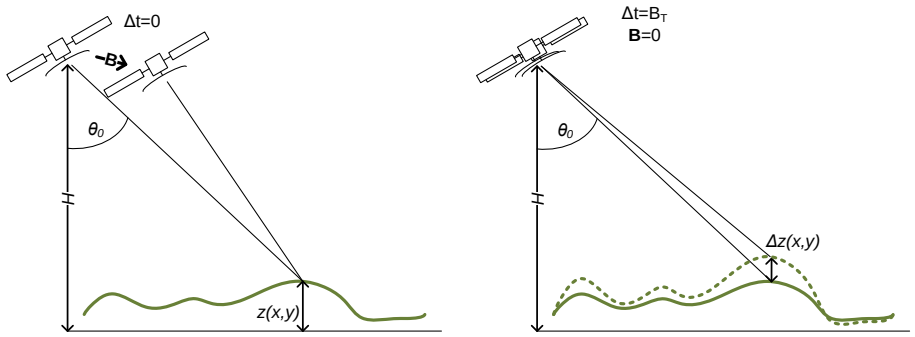

(a) Single-pass interferometry (b) Repeat-pass interferometry

Figure 2.6: Two main interferometric scenarios. Single-pass interferometry is used to measure surface height. Repeat-pass interferometry is used to measure the change in surface height. Here, Δt is the time between the acquisitions.

where ΔR is the change in distance to the scatterers between the acquisitions, and n is an integer related to the 2π phase ambiguity. The removal of this ambiguity is called *phase unwrapping*.

The *complex correlation coefficient* $\widetilde{\gamma}$ for polarisation PQ is defined as [36]:

$$\widetilde{\gamma}_{=}\gamma \mathrm{e}^{i\Delta\phi} = \frac{\left\langle S^1_{\mathrm{PQ}} \cdot S^{2*}_{\mathrm{PQ}} \right\rangle}{\sqrt{\left\langle \left|S^1_{\mathrm{PQ}}\right|^2 \right\rangle \left\langle \left|S^2_{\mathrm{PQ}}\right|^2 \right\rangle}} \tag{2.25}$$

where $\gamma = |\widetilde{\gamma}|$ is called *coherence*. Coherence is a real valued quantity between 0 and 1. It is a measure of the degree of similarity between the two images.

If the two acquisitions are made at the same time, but from slightly different positions, as in Figure 2.6(a), then it is possible to estimate the height of the surface $z(x, y)$, the digital surface model, from ΔR. This interferometric approach is called *single-pass interferometry*. It is most often used to create digital elevation models (DEMs), like the SRTM (USA) [37] and TanDEM-X (Germany) [38] missions.

If the two acquisitions are made at different times, but from the same positions, as in Figure 2.6(b), then it is possible to estimate the change of the surface $\Delta z(x, y)$ from ΔR. This is called *repeat-pass interferometry*. It is most often used to track topographic changes due to earthquakes and volcanoes. The ERS-1/2 (ESA) [39] mission and the new satellite constellation COSMO-SkyMed (Italy) [40] are good examples of satellite systems designed for repeat-pass interferometry[3].

Extended Covariance Matrix

The *extended covariance matrix* for the two images 1 and 2 is defined as:

$$[C_6] = \begin{bmatrix} \left\langle \underline{\mathbf{\Omega}}_1 \underline{\mathbf{\Omega}}_1^{\mathrm{H}} \right\rangle & \left\langle \underline{\mathbf{\Omega}}_1 \underline{\mathbf{\Omega}}_2^{\mathrm{H}} \right\rangle \\ \left\langle \underline{\mathbf{\Omega}}_2 \underline{\mathbf{\Omega}}_1^{\mathrm{H}} \right\rangle & \left\langle \underline{\mathbf{\Omega}}_2 \underline{\mathbf{\Omega}}_2^{\mathrm{H}} \right\rangle \end{bmatrix} = \begin{bmatrix} V_{11} & K_{12} \\ K_{12}^{\mathrm{H}} & V_{22} \end{bmatrix}, \tag{2.26}$$

where $[V_{11}]$ and $[V_{22}]$ are polarimetric covariance matrices for image 1 and 2 respectively, as defined in (2.21), and $[K_{12}]$ is as defined in (2.23).

[3] ERS-1/2 and COSMO-SkyMed are two systems consisting of more than one satellite designed for repeat-pass interferometry. However, two acquisitions from one satellite can also be used. In that meaning, almost all satellite systems are suitable for repeat-pass interferometry. However, the time between acquisitions can be too high to be able to extract valuable information.

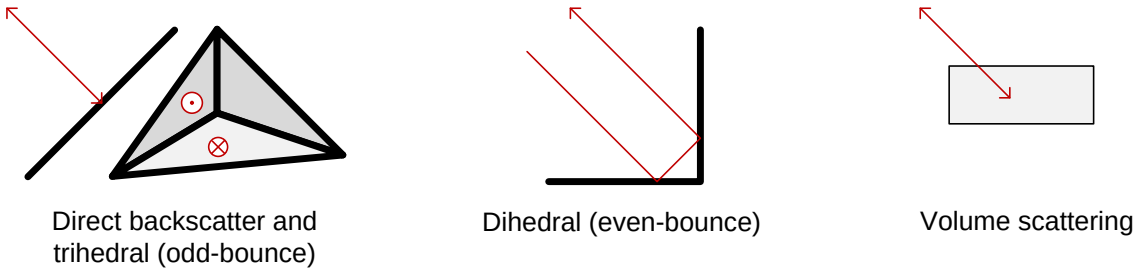

Figure 2.7: Illustration of the three basic scattering mechanisms.

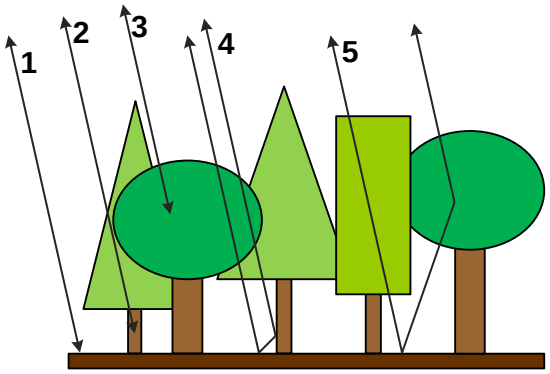

Figure 2.8: Basic scattering mechanisms for forests. 1: Direct backscatter from the ground. 2: Direct backscatter from the trunk. 3: Direct backscatter from the crown. 4: Ground-trunk or trunk-ground backscatter. 5: Ground-crown or crown-ground backscatter.

2.3 Radar Scattering

Basic Mechanisms

Electromagnetic waves can be scattered from objects in many different ways. The three most commonly distinguished scattering mechanisms are:

- single or odd-bounce scattering (eg. scattering from a plane surface or from a trihedral corner reflector),
- double or even-bounce scattering (eg. scattering from a dihedral reflector),
- direct backscatter from a volume of randomly oriented particles,

see also Figure 2.7. Each mechanism has different polarisation characteristics. For a metallic plate or a trihedral corner reflector oriented towards the incident electromagnetic field, scattering occurs in the same way for both horizontally and vertically polarised waves. No depolarisation occurs. For a horizontally oriented metallic dihedral, a phase shift of 180° is introduced between the vertical and horizontal polarisation, but no depolarisation occurs either. For a volume of randomly oriented particles, scattering occurs at different positions, and the scattered wave is incoherent. Moreover, strong depolarisation can be observed. Consult [33, 34] for more information on this topic.

Scattering from Forests

Radar scattering from forests is in general a complicated process. Forests are multi-scale targets, inhomogeneous in terms of structure and dielectric properties. As mentioned earlier, scattering characteristics are dependent on radar frequency. At lower frequencies, it is sufficient to only consider the large-scale elements,

such as tree stems, tree crowns, and the ground. However, at high frequencies, all elements such as leaves, needles, small branches, bark, and understorey vegetation contribute to scattering, making it more difficult to understand and model.

Nevertheless, a basic forest model consisting of the three elements ground, trunk, and crown can in many cases be sufficient. Using such simplified model, scattering from forests can be divided into five basic mechanisms [9]:

1. direct backscatter from the ground,
2. direct backscatter from the trunk,
3. direct backscatter from the crown,
4. ground-trunk or trunk-ground backscatter,
5. crown-ground or ground-crown backscatter,

see also Figure 2.8. Higher order scattering effects and multipath effects are less significant. Note, that the relation of the five mechanisms described above to the basic mechanisms presented in Section 2.3 is not always clear. For example, crown-ground backscatter may consist both of a dihedral reflection and volume scattering.

Using polarimetric decomposition theorems, the contribution of each basic scattering mechanism to the total backscattered field can be studied [33]. In Figure 2.9, *Pauli decomposition* is used to illustrate differences between P- and L-band SAR. Even-bounce scattering (mostly dihedral reflection) is shown in red, odd-bounce scattering (mostly direct backscatter and trihedral reflection) is shown in blue, and volume scattering is shown in green. Note, that Pauli decomposition is an approximative method for scattering mechanism discrimination. All conclusions should be made with care.

To illustrate the different scattering mechanisms, seven areas have been pointed out in Figure 2.9:

- A is a lake, and backscatter is very low in both P- and L-band, since all incident waves are reflected specularly away from the radar.
- B indicates a trihedral corner reflector, which gives a high intensity in the blue channel. Scattering from a trihedral is a triple-bounce effect, and therefore an odd scattering mechanism. Scattering at L-band is also stronger due to shorter wavelength/larger relative size of the reflector.
- C is a building consisting of two parts perpendicular to each other, and together with the ground, a trihedral is created. Also here, scattering is stronger at L-band.
- D is a building which together with ground creates a dihedral reflector, resulting in a high intensity in the red channel.
- E is a clear-cut where some trees were left for seeding. These trees can be clearly seen as lighter dots. The surface in a clear-cut is rough, and thus some direct backscatter can be seen in the blue channel. This backscatter is stronger at L-band because the roughness is more visible for shorter wavelengths.
- F is a forest, in which P-band SAR penetrates deeper. More double-bounce (trunk-ground or ground-trunk) backscatter can be seen in this region at P-band (more red colour). Also, less shadowing is visible in P-band due to smaller differences in height and better penetration at lower frequencies.
- G is partially a lake, but there is also some vegetation. P-band does not "see" the same structures as L-band.

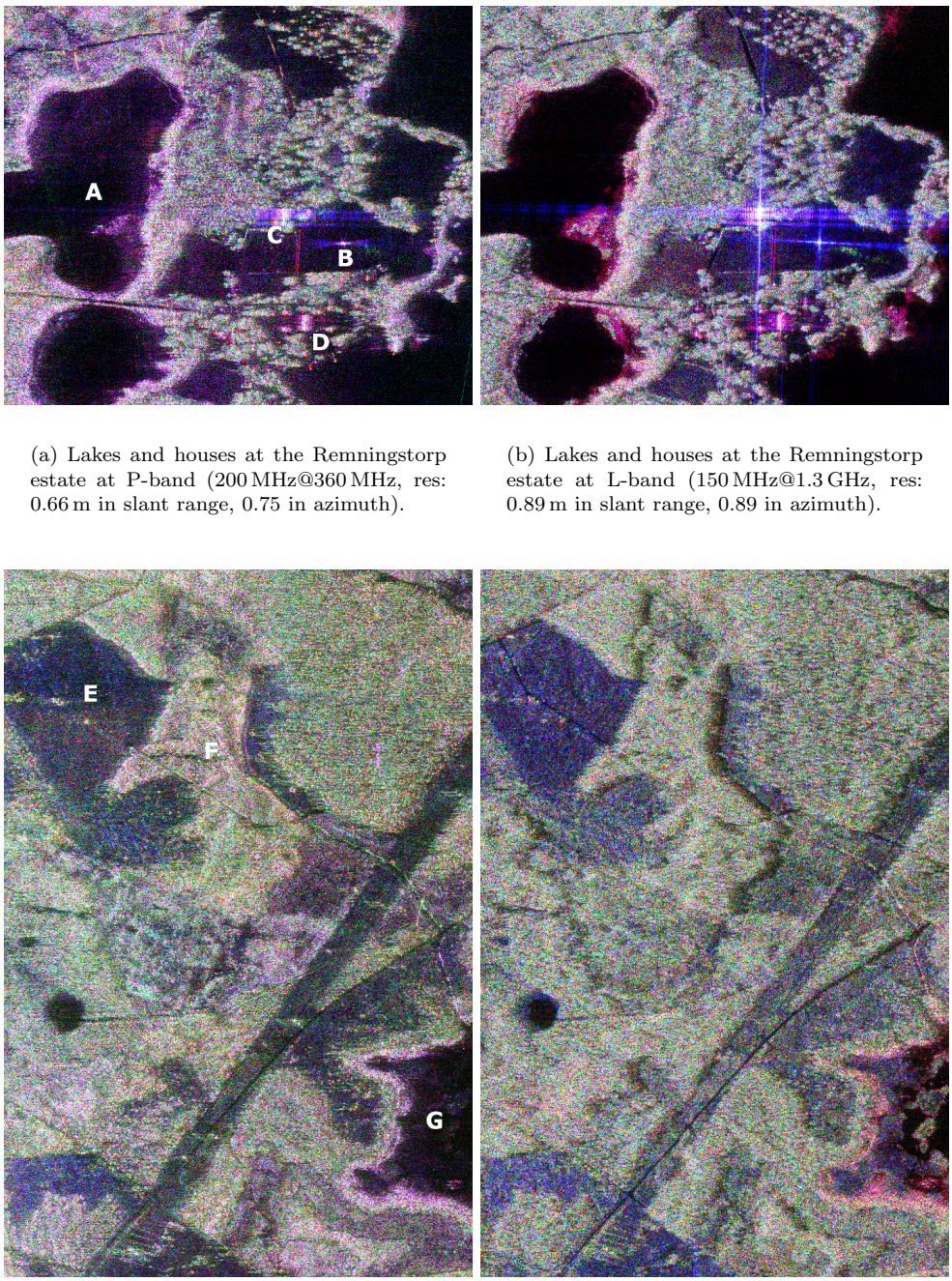

(a) Lakes and houses at the Remningstorp estate at P-band (200 MHz@360 MHz, res: 0.66 m in slant range, 0.75 in azimuth).

(b) Lakes and houses at the Remningstorp estate at L-band (150 MHz@1.3 GHz, res: 0.89 m in slant range, 0.89 in azimuth).

(c) Forested regions and clear-cuts at P-band (200 MHz@360 MHz, res: 0.66 m in slant range, 0.75 in azimuth).

(d) Forested regions and clear-cuts at L-band (150 MHz@1.3 GHz, res: 0.89 m in slant range, 0.89 in azimuth).

Figure 2.9: Comparison between P- and L-band SETHI images of Remningstorp from the BioSAR 2010 campaign [41, 42]. The pixel size is 1 m x 1 m. The nominal angle of incidence is around 57° for images (a) and (b) and around 45° for images (c) and (d). Colour composite images based on Pauli decomposition are shown here. Legend: HH–VV (mostly dihedral scattering), HV (mostly volume scattering), HH+VV (mostly direct backscatter and trihedral scattering). Note: histograms are matched for (a) and (b), and for (c) and (d), but the colour coding was chosen for best visual effect. The images should only be analysed qualitatively. Seven smaller areas discussed in the text are also marked in the P-band images.

Chapter 3

Summary of Appended Papers

In this chapter, the five papers appended to this thesis are summarised.

3.1 Paper A: Biomass Retrieval from P-band SAR Backscatter

In this paper, a new biomass retrieval model for boreal forest using polarimetric P-band SAR backscatter is presented. The model is based on two main SAR quantities: the HV backscatter gamma nought and the HH/VV backscatter ratio. It also includes a topographic correction based on the ground slope. The model is developed from analysis of stand-wise data from two airborne P-band SAR campaigns: BioSAR 2007 [43] (test site: Remningstorp, southern Sweden, stand-wise biomass range: 10–287 tons/ha slope range: 0–4°) and BioSAR 2008 [44] (test site: Krycklan, northern Sweden, stand-wise biomass range: 8–257 tons/ha, slope range: 0–19°). The new model is compared to five other models in a set of tests to evaluate its performance in different conditions.

All models are first tested on data sets from Remningstorp with different moisture conditions, acquired during three periods in the spring of 2007. Thereafter, the models are tested in topographic terrain using SAR data acquired for different flight headings in Krycklan. The models are also evaluated across sites, i.e. training on one site followed by validation on the other site. Using the new model with parameters estimated on Krycklan data, biomass in Remningstorp is retrieved with RMSE of 40–59 tons/ha, or 22–32 % of the mean biomass, which is lower compared to the other models. In the inverse scenario, the examined site is not well represented in the training data set and the results are therefore not conclusive. Biomass maps for Remningstorp and Krycklan are created using the new model, and compared to reference maps based on lidar scanning. The differences are pointed out and explained based on basic physics of scattering and observed conditions at the site.

Major part of the work presented in this paper was done within the feasibility study for the ESA BIOMASS mission.

3.2 Papers B, C, and D: Modelling of P-band SAR Data of Forests

In Paper B, a forward model for extended covariance matrix prediction for hemi-boreal and boreal forest in P-band SAR is presented. The main product is the extended covariance matrix scaled to sigma nought on the diagonal. The input parameters consist of basic radar setup, topography, forest biome, biomass, and some model parameters. Backscatter intensities for HH, VV, and HV channels are predicted from biomass using regression based on BioSAR 2007 campaign data. The phase of the correlation between the HH and VV channels is found to be proportional to biomass and is also modelled by a regression based on BioSAR 2007 data. The coherence of HH and VV channels is found to be unrelated to biomass and is chosen to

be modelled as a stochastic variable. The correlation of any co-polarised channel with HV is set to 0. The interferometric correlation values for the three channels are modelled using volume over ground (VoG) model, which is a combination of random volume over ground (RVoG), oriented volume over ground (OVoG), and elevated random volume over ground (ERVoG) models.

The forward model is also evaluated against SAR data from the BioSAR 2007 campaign [44]. Three intensity images and one complex polarimetric correlation image are created for Remningstorp (site of BioSAR 2007) from existing biomass map, DEM, and flight path information. These images are compared with the images acquired with ESAR during the BioSAR 2007 campaign and the similarities and differences are discussed. The presented forward model is able to predict backscatter with an RMSE of 1.4 dB (HV), 1.8 dB (VV), and 1.9 dB (HH). Polarimetric correlation can be predicted with magnitude and phase RMSE equal to 0.1 and 16°, respectively. A qualitative evaluation of the interferometric part is also done and it is concluded that a good setup of model parameters is necessary to get satisfactory results.

In Paper C, the forward model from Paper B is revised. Interferometric modelling is improved by the inclusion of suitable ground-to-volume ratios in the RVoG model. The ground-to-volume ratios are computed using the generalised Freeman-Durden polarimetric decomposition.

In Paper D, a tropical scenario is added to the forward model from Papers B and C. The tropical scenario is based on analysis of the data from the TropiSAR 2009 campaign [45].

The work presented in these papers was done within the feasibility study for the ESA BIOMASS mission. The forward model was integrated into the scene generation module, which was a part of the BIOMASS End-to-End Simulator [46].

3.3 Paper E: Detection of Wind-Thrown Forest and Clear-Cuts with L-, C-, and X-band SAR

A controlled experiment simulating wind-thrown forest was carried out at a hemi-boreal test site in Sweden. The simulation was done by manual felling of trees in September 2009. The trees were left on the ground until November 2009 to ensure image acquisitions after the simulated storm. SAR data from the satellites TerraSAR-X (X-band), RADARSAT-2 (C-band), and ALOS PALSAR (L-band) were acquired before, during and after this period. The backscatter signatures were analysed to evaluate possibilities to detect wind-thrown forest and clear-cuts. TerraSAR-X HH-polarised backscatter showed a significant increase when the trees were felled and the difference to selected reference forest stands was 1.2 dB to 2.0 dB. The corresponding differences for RADARSAT-2 were 0.2 dB to 1.2 dB for HH-polarisation and 0.1 to 1.1 dB for HV-polarisation. When the trees were felled, the ALOS PALSAR backscatter decreased to 1.6 dB below the reference forest for HH-polarisation and 0.4 dB to 0.8 dB for HV-polarisation. Shadowing effects in fine resolution TerraSAR-X and RADARSAT-2 data showed a high potential for detection of wind-throw with separation to the reference forest backscatter of between 4.9 dB and 9.2 dB. For clear-cut detection ALOS PALSAR proved to give the most suitable data.

Chapter 4

Conclusions and Future Work

4.1 Conclusions

The main scope of the work described in this thesis was to develop algorithms for extraction of valuable information from SAR data. As shown in Paper A, biomass could be extracted from airborne SAR with good results using an algorithm fitted to data from a different test site. By using two separate test sites, the robustness of the algorithm was tested. The use of the HH/VV-ratio together with the surface slope angle made the model significantly more stable compared to the other models.

In Papers B, C, and D, interferometric and polarimetric P-band SAR modelling for boreal and tropical forests was studied. Extended covariance matrix was predicted from a few parameters such as biomass, forest height, and the basic radar setup. The presented model was used to synthesise SAR images from biomass and height maps, and it showed good results.

In Paper E, SAR data from three satellites were used to evaluate the possibilities of storm damage and clear cut detection from space at different frequencies. A consistent change in backscatter could be observed at X-band when the threes were felled, possibly due to more specular reflections from the trunk. Also, when the trees were removed, a consistent change in backscatter could be observed at L-band. The study showed, that there are detectable changes at both X- and L-band.

4.2 Future work

Retrieval of forest biomass using P-band SAR should be further studied. Recently collected data from the BioSAR 2010 campaign, acquired in September 2010 in Remningstorp by the SETHI-platform should be studied together with the data from the first two BioSAR campaigns. Also, the algorithm should be studied on data from tropical forests, such as from the TropiSAR 2009 campaign conducted in French Guyana. A further development of the presented algorithm is desired. Inclusion of the slope aspect angle is a first step, but also the addition of some relevant polarimetric and interferometric indicators should be considered.

Modelling of the extended covariance matrix at P-band should be improved by the inclusion of topographic and temporal influence. The modelling of ground-to-volume ratios should be examined on more data. An extension of the low-frequency physical optics model presented in [47] for fully polarimetric data is also planned. This would not only aid forward modelling, but also improve the knowledge necessary for correct compensation of topographic effects in biomass retrieval models.

The study of storm damage and clear cut detection should be extended to polarimetry and/or interferometry. Also, an examination of both ascending and descending orbits, incident angles, and polarisations should be done in the future.

References

[1] World Wide Fund for Nature (WWF). (2012) Forests, jungles, woods & their trees. [Online, viewed 01 April 2012]. Available: http://wwf.panda.org/about_our_earth/about_forests/.

[2] IPCC, *Climate Change 2007: Mitigation of Climate Change. Contribution of Working Group III to the Fourth Assessment Report of the Intergovernmental Panel on Climate Change*, B. Metz, O. R. Davidson, P. R. Bosch, R. Dave, and L. A. Meyer, Eds. Cambridge, United Kingdom and New York, NY, USA: Cambridge University Press, 2007.

[3] P. Tans and R. Keeling. (2012) Trends in atmospheric carbon dioxide. [Online, viewed 29 March 2012]. Available: http://www.esrl.noaa.gov/gmd/ccgg/trends/.

[4] IPCC, *Climate Change 2007: The Physical Science Basis. Contribution of Working Group I to the Fourth Assessment Report of the Intergovernmental Panel on Climate Change*, S. Solomon, M. M. Dahe Qin, M. Marquis, K. Averyt, M. M. B. Tignor, and H. L. Miller, Eds. Cambridge, United Kingdom and New York, NY, USA: Cambridge University Press, 2007.

[5] C. Parker, A. Mitchell, M. Trivedi, and N. Mardas, *The Little REDD Book: A guide to governmental and non-governmental proposals for reducing emissions from deforestation and degradation.* Global Canopy Programme, John Krebs Field Station, Oxford OX2 8QJ, UK, November 2008.

[6] "Candidate Earth Explorer Core Mission: BIOMASS, Report for Assessment," European Space Agency (SP-1212/2), Tech. Rep., 2008.

[7] E. Næsset, T. Gobakken, S. Solberg, T. G. Gregoire, R. Nelson, G. Ståhl, and D. Weydahl, "Model-assisted regional forest biomass estimation using LiDAR and InSAR as auxiliary data: A case study from a boreal forest area," *Remote Sensing of Environment*, vol. 115, no. 12, pp. 3599–3614, 2011.

[8] T. Le Toan, A. Beaudoin, J. Riom, and D. Guyon, "Relating Forest Biomass to SAR Data," *IEEE Transactions on Geoscience and Remote Sensing*, vol. 30, no. 2, pp. 403–411, 1992.

[9] A. Beaudoin, T. L. Le Toan, S. Goze, E. Nezry, A. Lopes, E. Mougin, C. C. Hsu, H. C. Han, J. A. Kong, and R. T. Shin, "Retrieval of Forest Biomass from SAR Data," *International Journal of Remote Sensing*, vol. 15, no. 14, pp. 2777–2796, 1994.

[10] H. Israelsson, J. Askne, and R. Sylvander, "Potential of SAR for forest bole volume estimation," *International Journal of Remote Sensing*, vol. 15, no. 14, pp. 2809–2826, 1994.

[11] K. J. Ranson and G. Sun, "Mapping biomass of a northern forest using multifrequency SAR data," *IEEE Transactions on Geoscience and Remote Sensing*, vol. 32, no. 2, pp. 388–396, 1994.

[12] Y. Rauste, T. Häma, J. P. ans K. Heiska, and M. Hallikainen, "Radar-based forest biomass estimation," *International Journal of Remote Sensing*, vol. 15, pp. 1797–2808, 1994.

[13] M. L. Imhoff, "Radar backscatter and biomass saturation: ramifications for global biomass inventory," *IEEE Transactions on Geoscience and Remote Sensing*, vol. 33, no. 2, pp. 511–518, 1995.

[14] E. J. Rignot, R. Zimmermann, and J. J. van Zyl, "Spaceborne Applications of P Band Imaging Radars for Measuring Forest Biomass," *IEEE Transactions on Geoscience and Remote Sensing*, vol. 33, no. 5, pp. 1162–1169, 1995.

[15] D. H. Hoekman and M. J. Quiñones, "Land cover type and biomass classification using AirSAR data for evaluation of monitoring scenarios in the Colombian Amazon," *IEEE Transactions on Geoscience and Remote Sensing*, vol. 38, no. 2, pp. 685–696, 2000.

[16] S. Saatchi, K. Halligan, D. Despain, and R. Crabtree, "Estimation of Forest Fuel Load from Radar Remote Sensing," *IEEE Transactions on Geoscience and Remote Sensing*, vol. 45, pp. 1726–1740, 2007.

[17] G. Sandberg, L. M. H. Ulander, J. E. S. Fransson, J. Holmgren, and T. Le Toan, "L- and P-band backscatter intensity for biomass retrieval in hemiboreal forest," *Remote Sensing of Environment*, vol. 115, no. 11, pp. 2874–2886, 2011.

[18] S. Saatchi, M. Marlier, R. L. Chazdon, D. B. Clark, and A. E. Russell, "Impact of spatial variability of tropical forest structure on radar estimation of aboveground biomass," *Remote Sensing of Environment*, vol. 115, no. 11, pp. 2836–2849, 2011.

[19] T. Le Toan, S. Quegan, M. W. J. Davidson, H. Balzter, P. Paillou, K. Papathanassiou, S. Plummer, F. Rocca, S. Saatchi, H. Shugart, and L. Ulander, "The BIOMASS mission: Mapping global forest biomass to better understand the terrestrial carbon cycle," *Remote Sensing of Environment*, vol. 115, no. 11, pp. 2850–2860, 2011.

[20] M. J. Soja, G. Sandberg, and L. M. H. Ulander, "Biomass Retrieval for Boreal Forests in Sloping Terrain using P-band SAR Backscatter," Submitted to IEEE Transactions on Geoscience and Remote Sensing, February 2012.

[21] K. Folkesson, G. Smith-Jonforsen, and L. M. H. Ulander, "Model-Based Compensation of Topographic Effects for Improved Stem-Volume Retrieval From CARABAS-II VHF-Band SAR Images," *IEEE Transactions on Geoscience and Remote Sensing*, vol. 47, no. 4, pp. 1045–1055, April 2009.

[22] M. Moghaddam, Y. Rahmat-Samii, E. Rodriguez, D. Entekhabi, J. Hoffman, D. Moller, L. E. Pierce, S. Saatchi, and M. Thomson, "Microwave Observatory of Subcanopy and Subsurface (MOSS): A Mission Concept for Global Deep Soil Moisture Observations," *IEEE Transactions on Geoscience and Remote Sensing*, vol. 45, no. 8, pp. 2630–2643, August 2007.

[23] K. Scipal, M. Arcioni, J. Chave, J. Dall, F. Fois, T. Le Toan, C. Lin, K. Papathanassiou, S. Quegan, F. Rocca, S. Saatchi, H. Shugart, L. Ulander, and M. Williams, "The BIOMASS mission – An ESA Earth Explorer candidate to measure the BIOMASS of the Earth's forests," in *IEEE International Geoscience and Remote Sensing Symposium (IGARSS)*, Honolulu, HI, USA, July 2010, pp. 52–55.

[24] M. Arcioni, P. Bensi, J.-L. Bézy, B. Carnicero, M. Davidson, M. Drinkwater, F. Fois, A. Gabriele, R. Haagmans, F. Hélière, P. Ingmann, V. Kangas, M. Kern, S. Kraft, J. Langen, A. Lecuyot, C.-C. Lin, R. Meynart, K. Scipal, and P. Silvestrin, "Biomass, CoReH2O, PREMIER: ESA's candidate 7th Earth Explorer Missions," in *IEEE International Geoscience and Remote Sensing Symposium (IGARSS)*, Honolulu, HI, USA, July 2010, pp. 673–676.

[25] M. I. Skolnik, *Radar Handbook*, 2nd ed. McGraw-Hill, 1990.

[26] S. Kingsley and S. Quegan, *Understanding Radar Systems.* McGraw-Hill, 1992.

[27] W. G. Rees, *Physical Principles of Remote Sensing*, 2nd ed. Cambridge University Press, 2001.

[28] "IEEE Standard Letter Designations for Radar-Frequency Bands," *IEEE Std 521-2002 (Revision of IEEE Std 521-1984)*, 2003.

[29] R. J. Sullivan, *Radar Foundations for Imaging and Advanced Concepts.* Scitech Publishing, 2004.

[30] C. Oliver and S. Quegan, *Understanding Synthetic Aperture Radar Images.* Artech House, 1998.

[31] W. G. Carrara, R. S. Goodman, and R. M. Majewski, *Spotlight Synthetic Aperture Radar: Signal Processing Algorithms.* Artech House, 1995.

[32] I. G. Cumming and F. H. Wong, *Digital Processing of Synthetic Aperture Radar Data: Algorithms and Implementation.* Artech House, 2005.

[33] J.-S. Lee and E. Pottier, *Polarimetric Radar Imaging: From Basics to Applications.* CRC Press, 2009.

[34] F. T. Ulaby, C. Elachi, Y. Kuga, K. C. McDonald, K. Sarabandi, T. B. A. Senior, J. J. van Zyl, M. W. Whitt, and H. A. Zebker, *Radar Polarimetry for Geoscience Applications*, F. T. Ulaby and C. Elachi, Eds. Artech House, 1990.

[35] L. M. H. Ulander, "Radiometric Slope Correction of Synthetic Aperture Radar Images," *IEEE Transactions on Geoscience and Remote Sensing*, vol. 34, no. 5, pp. 1115–1122, 1996.

[36] S. R. Cloude, *Polarisation Applications in Remote Sensing.* Oxford University Press, 2010.

[37] T. G. Farr, P. A. Rosen, E. Caro, R. Crippen, R. Duren, S. Hensley, M. Kobrick, M. Paller, E. Rodriguez, L. Roth, D. Seal, S. Shaffer, J. Shimada, J. Umland, M. Werner, M. Oskin, D. Burbank, and D. Alsdorf, "The Shuttle Radar Tomography Mission," *Reviews of Geophysics*, vol. 45, 2007.

[38] M. Rodriguez-Cassola, P. Prats, D. Schulze, N. Tous-Ramon, U. Steinbrecher, L. Marotti, M. Nannini, M. Younis, P. Lopez-Dekker, M. Zink, A. Reigber, G. Krieger, and A. Moreira, "First Bistatic Spaceborne SAR Experiments With TanDEM-X," *IEEE Geoscience and Remote Sensing Letters*, vol. 9, no. 1, pp. 33–37, January 2012.

[39] E. Attema, G. Duchossois, and G. Kohlhammer, "ERS-1/2 SAR land applications: overview and main results," in *IEEE International Geoscience and Remote Sensing Symposium (IGARSS)*, Seattle, WA, USA, July 1998, pp. 1796–1798.

[40] A. Torre and P. Capece, "COSMO-SkyMed: The advanced SAR instrument," in *5th International Conference on Recent Advances in Space Technologies (RAST), 2011*, June 2011, pp. 865–868.

[41] L. M. H. Ulander, A. Gustavsson, P. Dubois-Fernandez, X. Depuis, J. E. S. Fransson, J. Holmgren, J. Wallerman, L. E. B. Eriksson, G. Sandberg, and M. J. Soja, "BioSAR 2010 - A SAR Campaign in Support to the BIOMASS Mission," in *IEEE International Geoscience and Remote Sensing Symposium (IGARSS)*, Vancouver, BC, Canada, July 2011, pp. 1528–1531.

[42] L. M. H. Ulander, A. Gustavsson, B. Flood, D. Murdin, P. Dubois-Fernandez, X. Depuis, G. Sandberg, M. J. Soja, L. E. B. Eriksson, J. E. S. Fransson, J. Holmgren, and J. Wallerman, "BioSAR 2010 Technical Assistance for the Development of Airborne SAR and Geophysical Measurements during the BioSAR 2010 Experiment: Final Report," ESA contract no. 4000102285/10/NL/JA/ef, Tech. Rep., 2011.

[43] I. Hajnsek, R. Scheiber, L. Ulander, A. Gustavsson, G. Sandberg, S. Tebaldini, A. M. Guarnieri, F. Rocca, F. Bombardini, and M. Pardini, "BioSAR 2007 technical assistance for the development of airborne SAR and geophysical measurements during the BioSAR 2007 experiment: Final report without synthesis," ESA contract no. 20755/07/NL/CB, Tech. Rep., 2008.

[44] I. Hajnsek, R. Scheiber, M. Keller, R. Horn, S. Lee, L. M. H. Ulander, A. Gustavsson, G. Sandberg, T. Le Toan, S. Tebaldini, A. M. Guarnieri, and F. Rocca, "BioSAR 2008 Technical Assistance for the Development of Airborne SAR and Geophysical Measurements during the BioSAR 2008 Experiment: Final Report - BioSAR Campaign," ESA contract no. 22052/08/NL/CT, Tech. Rep., 2009.

[45] P. Dubois-Fernandez, T. Le Toan, J. Chave, L. Blanc, S. Daniel, H. Oriot, A. Arnaubec, M. Rejou-Mechain, L. Villard, Y. Lasne, and T. Koleck, "TropiSAR 2009: Technical Assistance for the Development of Airborne SAR and Geophysical Measurements during the TropiSAR 2009 Experiment: Final Report," ESA contract no. 22446/09, CNES contract no. 9292903/08/09, Tech. Rep., 2011.

[46] P. Lopez-Dekker, F. De Zan, T. Borner, M. Younis, K. Papathanassiou, T. Guardabrazo, V. Bourlon, S. Ramongassie, N. Taveneau, L. Ulander, D. Murdin, N. Rogers, S. Quegan, and R. Franco, "BIOMASS end-to-end mission performance simulator," in *IEEE International Geoscience and Remote Sensing Symposium (IGARSS), Vancouver, BC, Canada*, July 2011, pp. 4249–4252.

[47] B. Hallberg, G. Smith-Jonforsen, L. M. H. Ulander, and G. Sandberg, "A physical-optics model for double-bounce scattering from tree stems standing on an undulating ground surface," *IEEE Transactions on Geoscience and Remote Sensing*, vol. 46, no. 9, pp. 2607–2621, 2008.